International Journal of Engineering Trends and Technology
ISSN: 2231–5381 / https://doi.org/10.14445/22315381/IJETT-V71I5P242

Volume 71 Issue 5, 422-434, May 2023

Original Article

Physical and Ferri Magnetic Properties of Copper Doped NiZn along with Iron Excess Ni-Zn Ferrites Yielded by Co-Precipitation Method

S. Sri Surya Srikanth[1], B. Rajesh Kumar[2]

[1,2]*Department of EECE, GITAM Institute of Technology, GITAM (Deemed to be University)*

[1]*Corresponding Author : ssathira20@gmail.com*

Received: 21 November 2022 Revised: 02 February 2023 Accepted: 06 May 2023 Published: 25 May 2023

Abstract *- Nickel Zinc ferrite compounds are generally used as gas sensing materials. Thinfilm sensors are developed using doped copper Nickel, Zinc, and iron excess NiZn ferrite integrated by co-precipitation method utilizing NaOH as a precipitating agent. The process and development of NiZn ferrite pellets have been presented in this paper. Samples are characterized using XRD, FT-IR, Raman, and VSM. The XRD shows the levels of diffraction peaks (220), (311), (222), (400), (422), (511), and (440). The FTIR, Raman, and VSM give the physical properties, i.e., single spinel phase is confirmed by FTIR and Raman spectra, VSM shows the magnetic behavior of NZF nanoparticles, Ferrite nanoparticles energy band gap is measured using UV-Vis spectroscopy to make the pellets suitable for gas sensing applications. As a result, there is a more number of nickel ions, and 10% of the net doping concentration of copper ions at the A-site is not a size-dependent phenomenon and adding an excess of iron leads to better sensitivity.*

Keywords *- NiZn ferrite, Cation retention, Elastic specifications, Cation dissemination, Rietveld investigation.*

1. Introduction

The current scenario focuses on human considerations and environmental monitoring for safety. Air pollution has been rising in recent years because of population growth in cities and the production of vehicles and other sources of pollution. So the development, characterization, and application of nanomaterials for gas sensing have been encouraged because of their many potential uses in adsorption, separation, catalysis, and sensors. [1]. Since their typical, outstanding magnetic and electrical characteristics, nanocrystalline spinel ferrites are materialistically noteworthy. Scholars and academics have been drawn to nano ferrites for various reasons, including catalysts, gas sensors, targeted medication delivery, and spintronics. [2]. The present trend focuses on personage health and climatic safety monitoring. Daily air pollution has grown dramatically in recent years because of increasing urbanization. Many autos produce enormous quantities of pollutants such as gases, volatile chemical compounds, and particulate components, among other things. As a result, scientists, technologists, and technophiles have opted to manage the decomposition of air using a range of schemes to protect, regulate, and reduce pollution.[3] The spinel ferrite has the general chemical prescription AB_2O_4 and is a type containing oxygen and cations that are finally distributed at the tetrahedral [A] and octahedral [B] slots [4,5]. The aim of this study is to investigate the effect of stoichiometric compositional changes of NiZn spinelliferrite on the stoichiometric, optical and ferromagnetic properties caused by the replacement of Ni_2 by divalent Cu_2. The architectural, linguistic, magnetic and DC properties of Ni-Zn spinel ferrite nanoparticles are replaced by the chemical formula $Ni_{0.65-x}$ $Zn_{0.3}Cu_xFe_2O_4$[6,7] is prepared by co-precipitation, and the chemical formula restores the magnetic and DC properties of architectural, lingual Ni-Zn spinel ferrite nanoparticles. The copper exchange of $Ni_{0.65-x}$ $Zn_{0.3}Cu_xFe_2O_4$ has been presented as a target for computational heritage [8].

2. Experimentation & Characterization

2.1. Preparation of NZF Pellets

Here, all analytical geometry reagents were recycled without sanctification [9,10]. The primary ingredient such as Nickel(II) nitrate hexahydrate($Ni(NO_3)_2.6H_2O$),(98.5%), Zinc nitrate hexahydrate ($ZnN_2O_6.6H_2O$),(98%), Copper(II) nitrate trihydrate ($CuN_2O_6.3H_2O$),(>=98%), and iron(III) nonahydrate $Fe(NO_3)_3.9H_2O$),(>98%) were supplied from pure synth research chemicals, India are combined separately with a minimal quantity of deionized water in stoichiometric ratios sufficient for a particular solid phase reaction. Chemically co-precipitation is used to construct tiny polycrystalline particles of spinel ferrites. $Ni_{0.65-x}Zn_{0.35}Cu_xFe_2O_4$ and $Ni_{0.65-x}Zn_{0.35}Cu_xFe_{2.05}O_4$ (x = 0.0, 0.15) [11]. These are referred to as NZ1, NZ2, NZ3, and NZ4, respectively. The underlying criterion was the outstanding purity of poorly soluble zinc and iron (III) in the quality of analytical reagents. The synthesis process flow of Ni-Zn ferrite nanoparticles is shown in Figure 1 [12,13]. It has been presented as a target for computer-assisted inheritance [8].

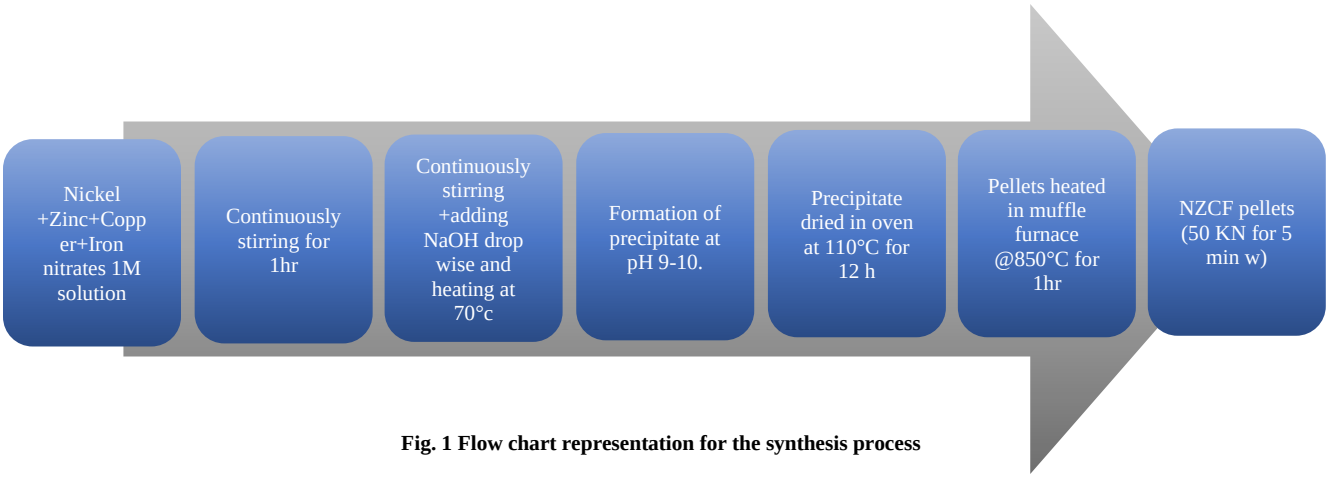

Fig. 1 Flow chart representation for the synthesis process

3. Characterization methods

The physical parameters of NZF pellets, such as particle size, density, porosity, stiffness constant, and elastic moduli, were examined using Scherrer, Williamson Hall, Size Strain-Plot, and Halder-Wagner-Plot, Tauc's plot methods. CuK radiation (= 1.5405; 10-800) was utilised to assess ferrites using a PW1710 Philips X-ray diffractometer. (XRD). On a Perkin Elmer Spectrum in India, the FTIR spectra of fine samples of all compounds were collected using 1:3 KBr as a solvent for all samples between 4000 cm-1 and 400 cm-1. The surface of the collected powder sample was detected using a field emission scanning electron microscope (FESEM) with the SIGMA HV version (magnification range x50-one hundred,000X). A vibrating sample magnetometer (VSM: PAR EG & G 4500) was used to obtain magnetic measurements up to a magnetic terrain of 15 kOe at a certain ambient temperature.

4. Results & Discussions

As illustrated in Fig 2, all specimens solidified at 850ºC have been subjected to X-Ray diffraction.

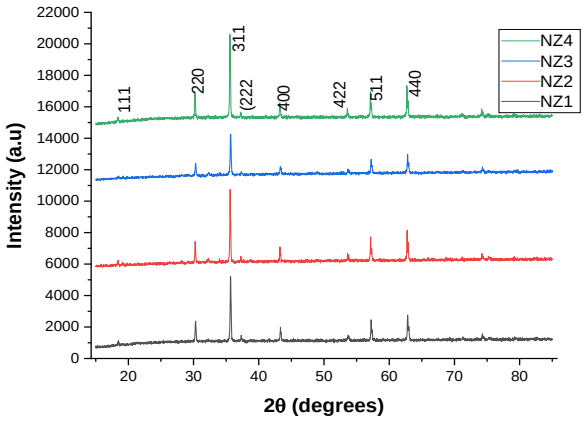

Fig. 2 XRD patterns of Cu substituted Ni-Zn ferrite samples.

X-ray diffraction (XRD) (Rigaku Smart lab, 3KW, India) was used to estimate the crystallite size using CuK radiation with a 2θ angle ranging from 5 to 80°. The miller indices (hkl) have been assigned to diffraction peaks by comparing 2θ values and measured d-values with standard d-values. The diffraction planes (220), (311), (222), (400), (422), (511), and (440) at the highest diffraction intensity. In all samples, a cubic spinel structure can be recognized in the (311) plane. The lattice parameter calculation has been made from each peak of the X-ray pattern using the equation [14,15] and diffraction angle θ. Nelson-Riley function, to the analysis of lattice parameter, is given by equation.

$$F(\theta) = \frac{1}{2}\left(\frac{cos^2\theta}{sin\theta} + \frac{cos^2\theta}{\theta}\right) \quad (1)$$

A precise lattice constant determination was achieved by projecting the estimated lattice parameters to the Nelson-Riley function. This function has a zero process. The lattice parameter (a) rises from 8.38015 Aº to 8.38448 Aº as the copper concentration rises. Table 1 illustrates the Lattice constant for Ni-Zn ferrite samples.

Table 1. Lattice constant table for Ni-Zn ferrite samples

Composition	a(Aº)
NZ1	8.38015
NZ2	8.38329
NZ3	8.38328
NZ4	8.38448

The rise in lattice monophonic [41] is due to the high ionic radii (0.74Aº) of copper instead of nickel ion (0.69Aº). The increase in copper affects the crystallite intensity (D). This can be approximated by judging from the data obtained by FWHM (β). The peak spread is known to depend on the effect of the instrument operation, crystallite size, and the stress effects within the crystal lattice. These coefficients can be calculated using equation (4). Estimate and analyze the factors that

influence equations (2) & (6), the crystallite size (D) (shown in the preliminary category).

Figures 3, 4, and 5 illustrate how the crystallite magnitude is predicted using the Scherrer, Williamson Hall, Size Strain-Plot schemes [17] and Halder-Wagner-Plot [18] approaches.

The crystallite size of all specimens is determined using the Scherrer equation (Eq. (2)) [19], and the full width at half-maximum intensity is derived from the XRD patterns. The Scherrer equation is as follows:

$$D = \frac{0.89\lambda}{\beta cos\theta} \quad (2)$$

Here, D denotes the size of the crystallite (nm), the constant k built into the crystallite's outline, the half diffraction angle (rad), the FWHM intensity, and the wavelength of the X-ray (0.154nm).

Scherrer's equation considers the crystallite effects and leaves behind the intrinsic strain caused by grain barriers, point faults, stacking defects, and threefold junctions. The W-H scheme deal with the joint enact proportion and strain-induced expansion, which can be conveyed as

$$\beta cos\theta = \left(\frac{k\lambda}{D}\right) + (4\varepsilon sin\theta) \quad (3)$$

The slope in Eq.3 between the 4εsinθ (X-axis) and βcosθ (Y-axis) terms is parallel to a specific diffraction peak, indicating elongation and intersections show the mean crystallite content.

The Size-Strain plot (SSP) is yet another method for considering the Lorentzian function of an XRD profile with increasing size enhancement and the set of Gaussian function characteristics of an XRD profile with increased extension [20]. SSP computes the following formulation's usage:

$$(d\beta cos\theta)^2 = \left(\frac{k\lambda}{D}\right) + (d^2\beta cos\theta) + \left(\frac{\varepsilon^2}{4}\right) \quad (4)$$

where d represents the interplanetary gap of each crest, in equation 4, the slope of the plot between the terms d^2 βcosθ (X-axis) and $(d\beta cos\theta)^2$ (Y-axis) corresponds to each diffraction crest and represents the mean crystalline content and the intersection point represents an inherently significant strain.

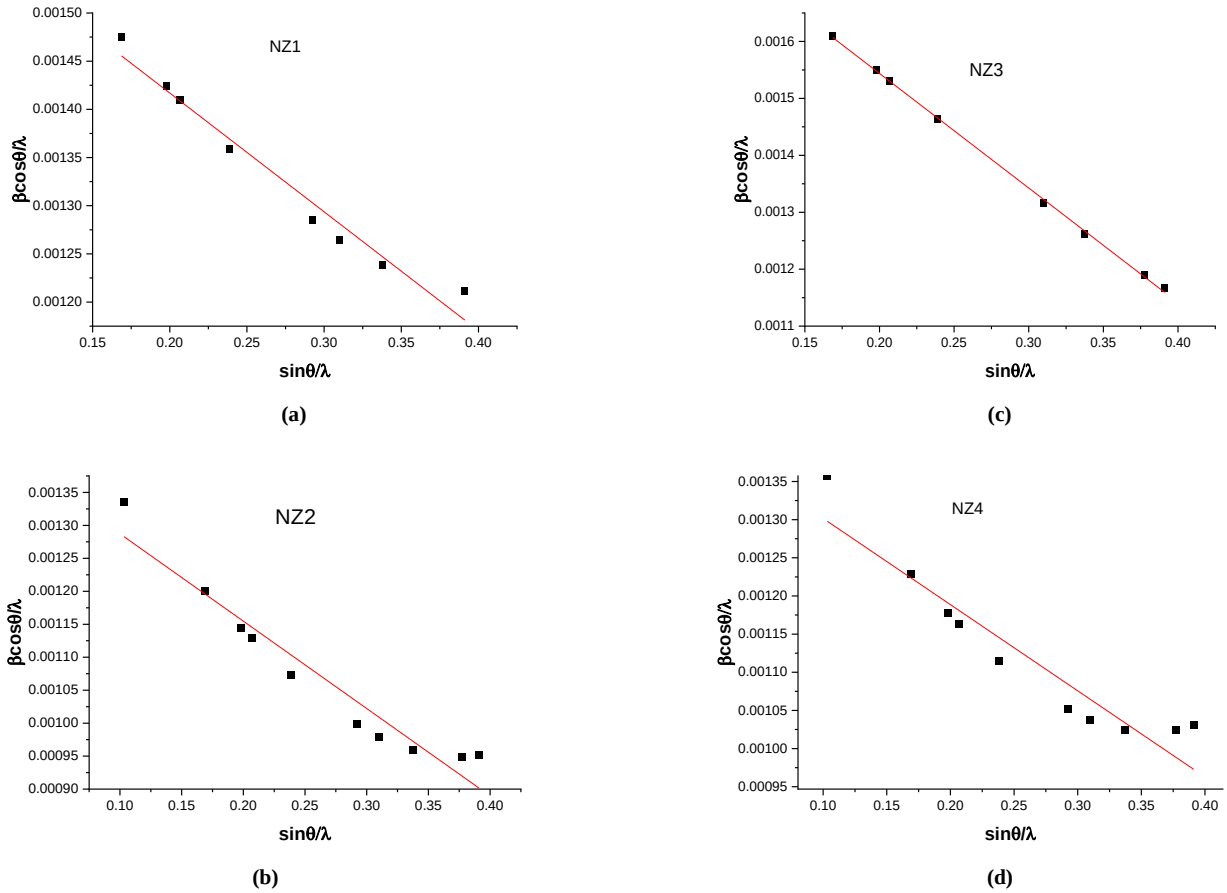

Fig 3(a-d) Williamson-Hall plots for Ni-Zn ferrite samples i.e., NZ1, NZ2, NZ3 and NZ4

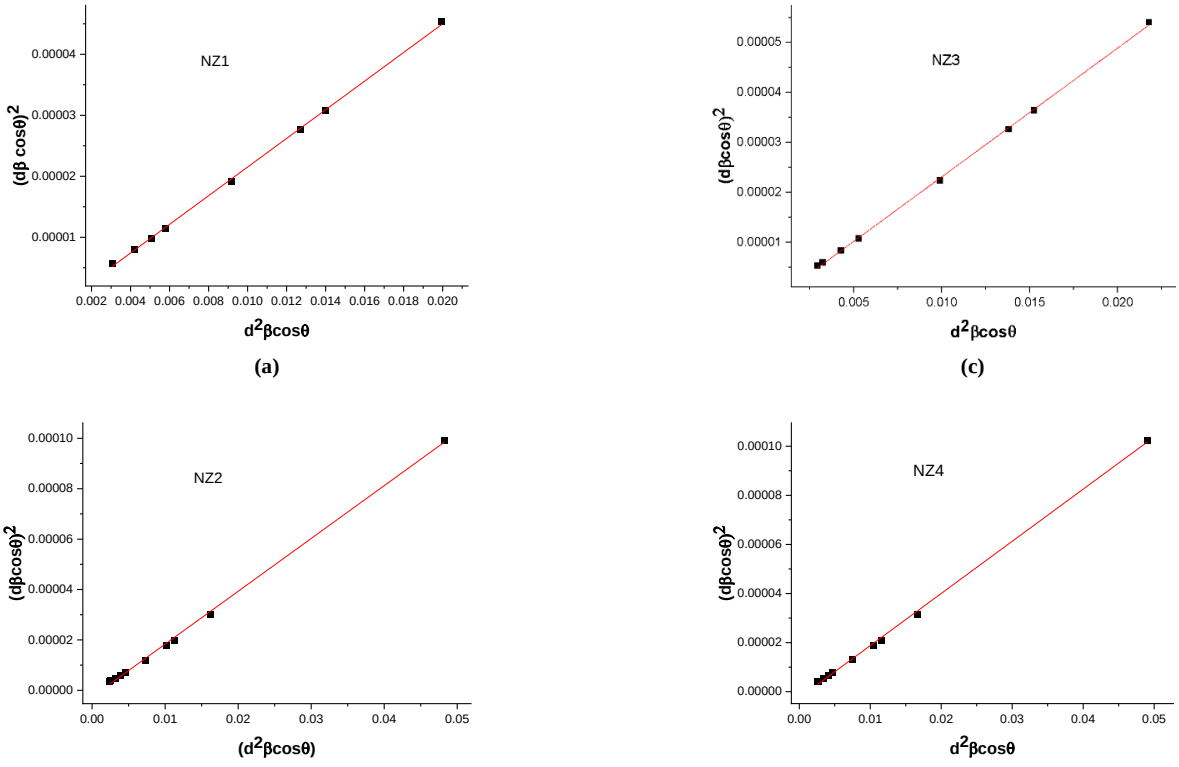

Fig 4(a-d) Size strain plots for NZCF samples i.e., NZ1, NZ2, NZ3, and NZ4

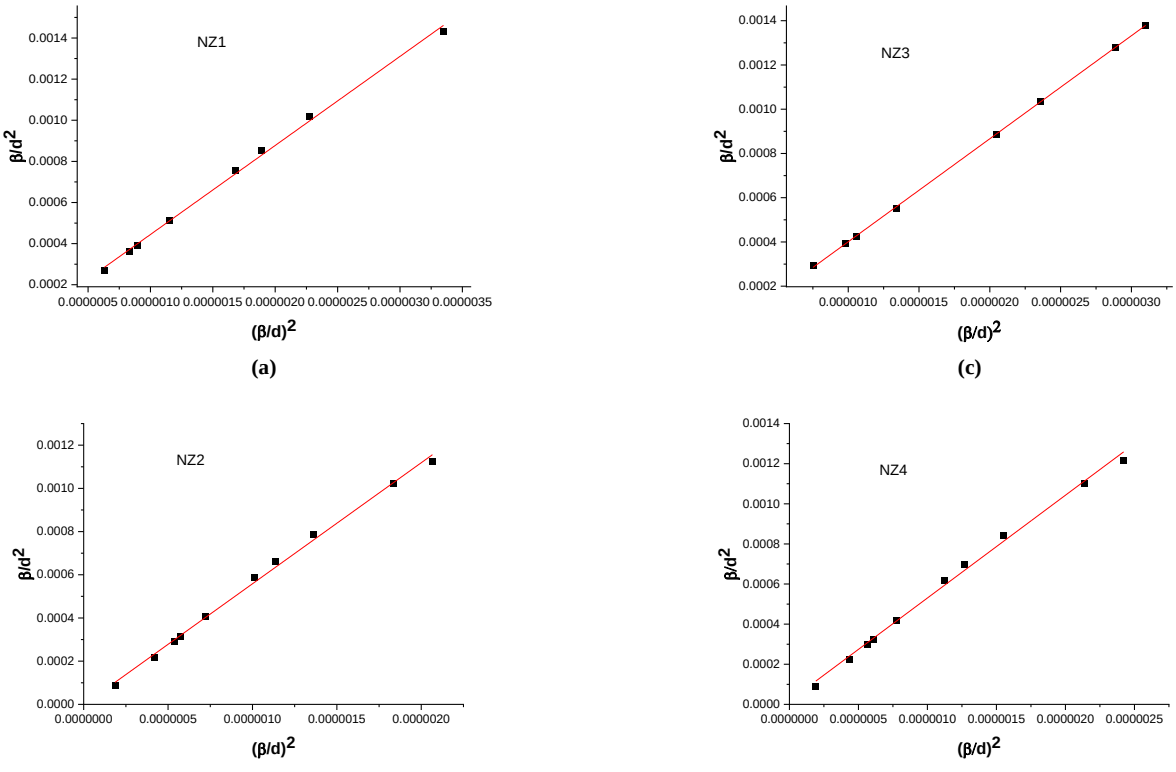

Fig. 5(a-d) Halder-Wagner plots for Ni-Zn ferrite samples i.e NZ1, NZ2, NZ3 and NZ4

The SSP method assumes that the magnitude distribution of the XRD peak profile is a Lorentz function, and the magnitude distribution is a Gaussian function because it agrees well with the Gaussian function. In comparison fails quickly without adjustment [21,22]. On the other hand, the tail portion of the profile matches the Lorentz position very well but does not meet the XRD crest area. To conquer these difficulties, the Halder-Wagner method is recycled. This suggests that the peak extension is an asymmetric Voigt function. For the Voigt function, we can use Halder-Wagner Method to write the full width of the maximal half value as follows:

$$\beta^2 = \beta_L \cdot \beta_{hkl} + \beta_G^2 \quad (5)$$

This technique, where β_L and β_G are the full widths half maximum of the Lorentz and Gaussian functions, lends more weight to the peaks in the tiny and medium-angle versions, where the diffraction peaks have little or no overlap. According to the Halder-Wagner Method, the following is the relationship between crystallite peak and lattice constant.

$$\left(\frac{\beta^*_{hkl}}{d^*_{hkl}}\right) = \frac{1}{D}\frac{\beta^*_{hkl}}{d^{*2}_{hkl}} + \left(\frac{\varepsilon}{2}\right)^2 \quad (6)$$

Figure 5 shows a plot of β/d^2 term along the X-axis and $(\beta/d)^2$ terms onward the intrinsic Y-axis for individual peaks in the XRD pattern.

The interception reflects the intrinsic strain of the NiZn ferrite specimen and the inclination is directly drawn delineation depicts the overall size. The crystallite size and intrinsic strain agree well with the SSP model; however, the pressure value derived from the Halder-Wagner plots is five times more than the elongation value obtained from other fashions: all the computed crystallite size D(nm) and intrinsic strain values. The crystallite size D determined using the W-H, SSP, and H-W techniques are clearly identical, as shown in Table 2.

The Scherrer technique summarizes several modified versions of the Williamson-Hall (WH) equation's strain plot[24,25]. The lattice strain is calculated using modified W-H models, as shown in Figures 3, 4, and 5, and the SSP techniques may be compared. Furthermore, the average crystallite size of Ni-Zn samples from different models is close to closer values.

When a Raman mode (e.g., M-O4) has a pair of cation forms, the resultant peaks have broad peaks with symmetrical contributions from additional cations. Consequently, the cliffs form appropriately, and the integrated intensity beneath each sub-peak provides a measure of the unit cell's cation concentration [41]. Raman spectra were recorded within the scene of 100-1000 cm-1 at room temperature for the taking after pellet compositions, and the created run of each example appears shown in Fig.6.

Table 2. Crystallite size of Cu doped and iron excess Ni-Zn ferrites calculated using different methods.

Composition	Scherrer method	W-H method		Size strain plot		H-W method	
	D(nm)	D(nm)	Strain ξ	D(nm)	Strain ξ	D(nm)	Strain ξ
NZ1	52.94	83.5	0.12×10^{-6}	59.21	0.00824	43.47	1.79×10^{-6}
NZ2	64.28	97.64	0.13×10^{-6}	66.02	0.07483	56.17	0.52×10^{-6}
NZ3	47.36	71.1	0.20×10^{-6}	53.74	0.08717	46.51	0.23×10^{-6}
NZ4	64.28	98.33	0.11×10^{6}	65.4	0.07483	51.54	0.34×10^{-6}

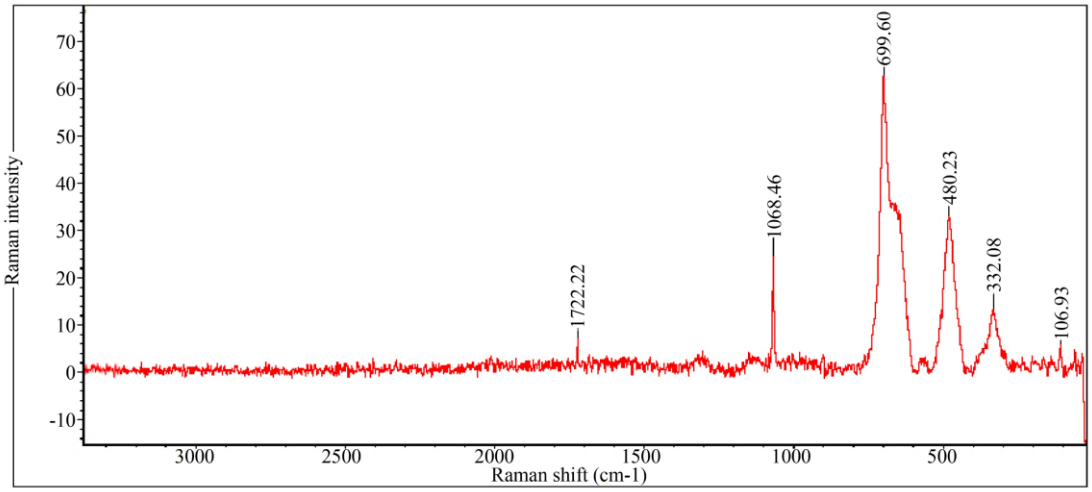

(a)

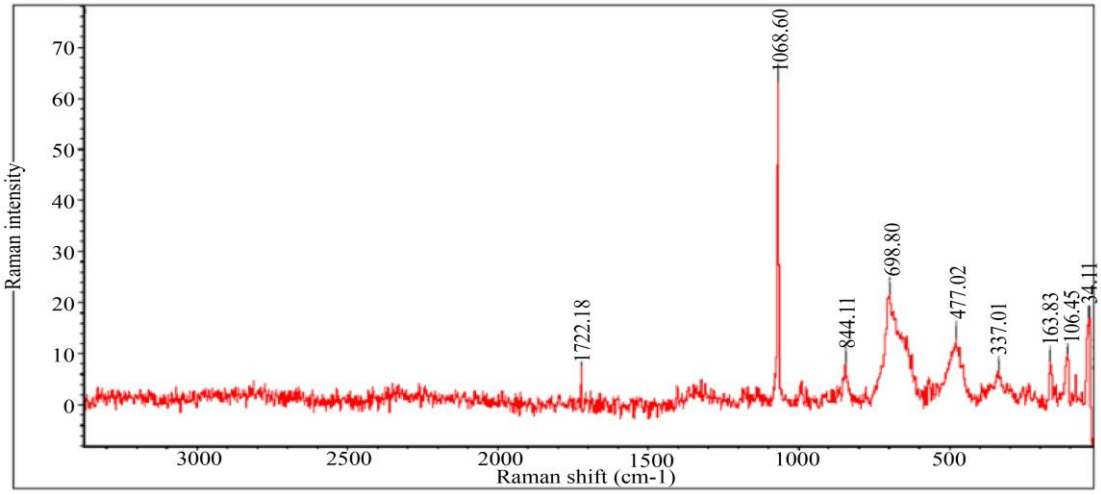

(b)

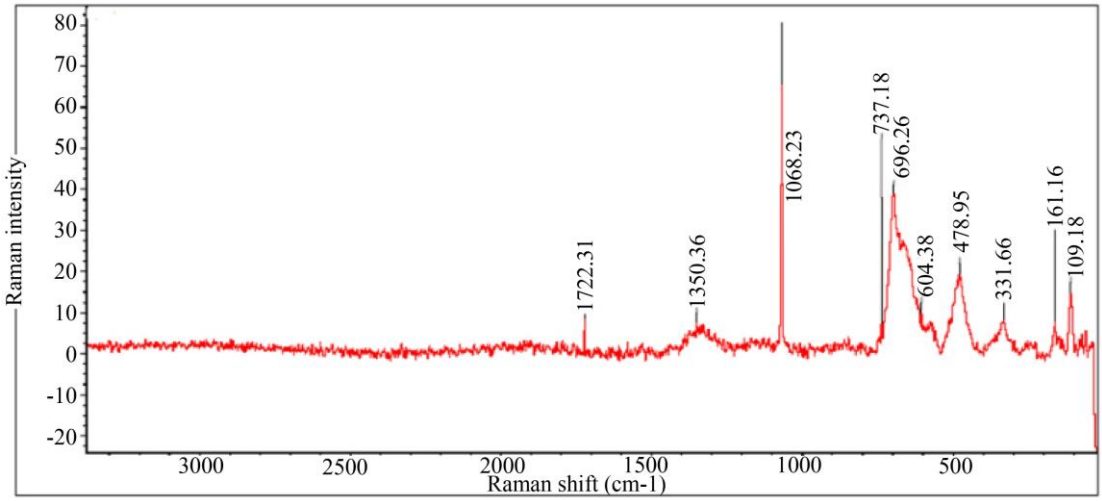

(c)

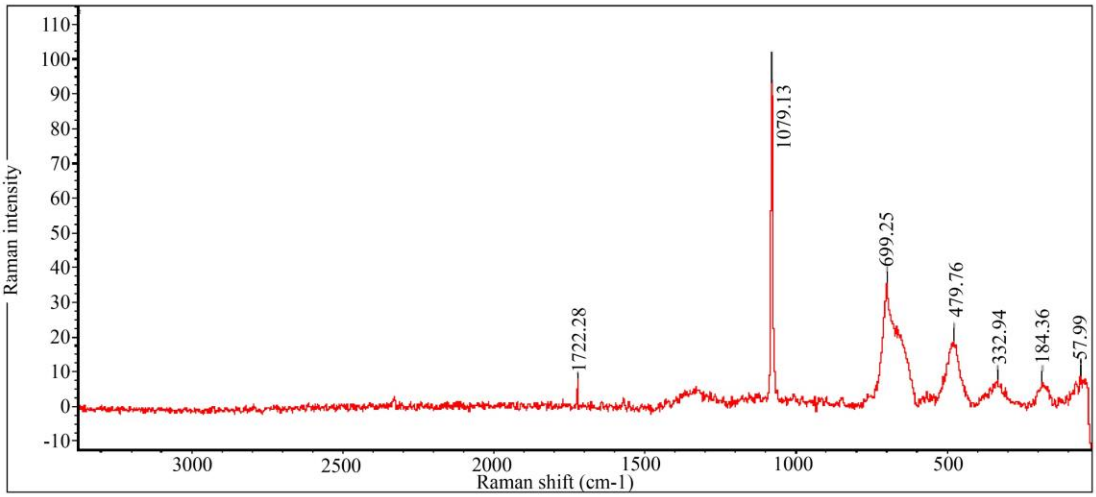

(d)

Fig 6(a-d) Raman shift for copper-substituted ferrite samples of NiZn, i.e. NZ1, NZ2, NZ3 and NZ4

Table 3. Active Raman modes (Eg, T2g, A1g) Band Frequencies and Mode Assignments

Sample	Eg	I_{Eg}	$T2_{g\,(2)}$	$I_{T2g\,(2)}$	$A1_{g\,(2)}$	$I_{A2g(2)}$
NZ1	332	13.3	480	32.8	699	62.8
NZ2	337	6.7	477	13.1	699	21.4
NZ3	332	8.1	479	19.2	696	39
NZ4	333	7.3	477	18.9	699	35.6

NiZn ferrite with Fd3m spinel structure yields 39 standard rules. Five of these (A1g+Eg+3T2g) are Raman active [13]. Nickel-zinc ferrite samples had broadbands at 331, 480, and 699 cm-1 [14]. The observed Raman bands are normal oscillations that reveal the polycrystalline single-phase structure of NiCuZn spinel ferrite. The cubic phase is projected to have active Raman peaks as high as A1g, Eg, and T2g, as seen in the spectrum of content. Despite the other two T2g modes, distinguishing the plot distribution in the range was difficult. The Raman band at 690 cm–1 is assigned to A1g(2), 480 cm–1 is assigned to T2g(2) as shown in Table 3, and 332 cm–1 is assigned to Eg modes, which reflects vibration at the tetrahedral sites (T-site) [52]. All samples show almost the same pattern of Raman spectra. With the expectation of basic Ni-Zn ferrite, a decrease in peak intensity was observed. These observations indicate that the cation has changed from tetrahedral to octahedral sites. These changes may be due to the rise from a high cation disorder induced by Cu2+ and Fe2+ ions and the strong cation perturbations caused by the particle size effect. [8].

4.1. Fourier Transforms Infrared Spectroscopy

Table 4. FTIR composition and wavenumber of the sample

Composition	υ_T (cm^{-1})	υ_o (cm^{-1})	F_T (Nm^{-1})	F_o (Nm^{-1})
NZ1	590	423	255	131
NZ2	588	421	253	130
NZ3	590	421	253	128
NZ4	584	425	249	131

Fourier Transform Infrared Spectroscopy (FTIR) may be used to analyze[26] ion redistribution between sites A and B, as predicted, utilizing lattice constants, lengths, and voltage changes as rises. Figure 7 shows the FTIR spectra of all of the pellets.

The redistribution of cation ions is shown by a consistent drop in both wavenumbers equal to A and B sites [Table 4]. As copper concentrations rise, new settings of nickel, zinc, iron, and other elements may form, reducing the wavenumber at both locations. Varieties in drive constant[42], bond lengths, and Debye temperature[28,29] may be utilized to assist in recognizing the issue of cobalt in NiZn ferrites.

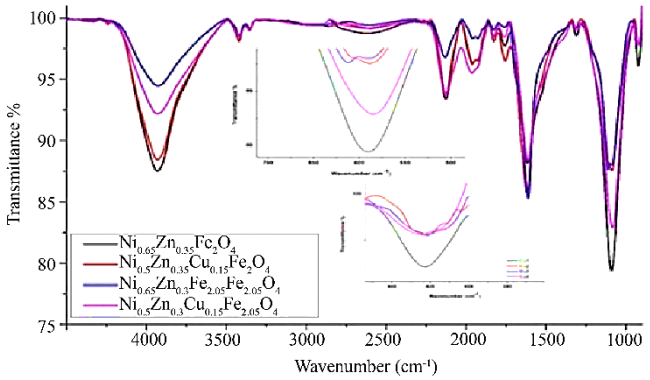

Fig. 7 FTIR absorption spectra of $Ni_{0.65-x}Cu_xZn_{0.35}Fe_2O_4$ and $Ni_{0.65-x}Cu_xZn_{0.3}Fe_{2.05}O_4$ (x= 0, 0.15) ferrites

The distribution of copper ions at both A and B-sites, together with concomitant readjustments in cation distributions of nickel and iron ions in the spinel lattice, may be ascribed to the observed changes in wavenumbers υ1 & υ2 and the drop in force constant values. Nickel with copper may occupy both A/B sites because zinc favors A-sites over B-sites. Copper ions are present at both A and B-Sites, as shown by variations in FTIR spectrum and XRD intensity. At 584-612 cm^{-1} and 421-435 cm^{-1}, the two large crests correspond to tetrahedral and octahedral sites of Fe-O stretching vibrations, respectively. Single-phase spinel ferrites are known for their absorption bands. [30,31].

Using the band frequencies from the FTIR study, the FTIR spectra of all compositions shown in Figure 7 and the tetrahedral site (K_T) and octahedral site (K_o) force constants are substituted into the following standard equations. It is obtained by

$$K = 4\pi^2\, c^2 \upsilon^2 \mu \tag{7}$$

$$\mu = \left(\frac{M_O\, X\, M_{Fe}}{M_O + M_{Fe}}\right) \tag{8}$$

where wavenumber is represented by υ , speed of mass is denoted by c, effective mass is denoted by μ, atomic weights of O and Fe corresponds to M_o and $M_{Fe.}$

Poisson's ratio, elastic stiffness constants C_{11}, C_{12}, elastic constants Young's modulus (E), Rigidity modulus (G), Rigidity modulus (G), longitudinal elastic wave velocity V_l, shear wave velocity $V_{s.}$, mean wave velocity V_m, and θ_D is Debye temperature is obtained using the relationships mentioned elsewhere [15].

In the theoretical range, Poisson's ratio values show a slight decrease from 0.259 to 0.272 with increasing copper concentration(x). Table 5 shows the Elastic constant along with the stiffness constant, but the copper content is slightly reduced. This slight depletion of elastic moduli is due to the negligible diminishing of interatomic bonds out of all the atoms in the spinel lattice with copper grouping.

From Table 5, it has been observed that the study of elastic properties for spinel ferrite. The change in wave velocities (see Table 6) shows that the value of the longitudinal wave velocity V_l decline in the concentration of cobalt, meantime is the shear wave acceleration Vs decreases. The average wave velocity Vm is indicated as a delineator.

Substitution of copper reduces the elastic wave velocity due to lattice vibration enhancement [39] and limits the elastic modulus. Debye temperature is defined as the occurrence of lattice vibrations at a known temperature. From these tables, we can see that K, E, and G decrease with increasing copper content (x). The change in K, E, and G values due to copper content (x) can be explained by considering the atomic bond. From this, it can be concluded that the interatomic bond among the atoms is continuously depleted in use to rise in elastic modulus with the concentration (x). The poisons ratio (σ) value was found to be constant in all the samples. In addition, these values range from 0.26 to 0.27, consistent with the theory of isotropic elasticity. Increasing lattice vibration reduces the speed of the elastic wave, which leads to a decrease in elastic moduli during copper exchange.

4.2. UV-vis Studies

The optical theory of semiconducting nanocrystals is examined by using a UV-visible spectrum. The E_g(bandgap) for the as-synthesized material was determined by Tauc's plot (Fig. 8). In view of the absorption spectrum of $NiFe_2O_4$ nanoparticles in both as-prepared and annealed states at various temperatures.

The absorption spectra of both samples have a narrow primary peak and were found below 370 nm. This shows that there is a probability of observing photo luminesce emission for an excitation wavelength of 370 nm. The reflectance data has been used to estimate the bandgap of the material sample using a modified Tauc's plot [17], i.e. fig .9(a-d), employing the modified Kubelka-Munk equation [20].

$$[F(R\infty)h\upsilon]^2 = C_2(h\upsilon - E_{gap}) \quad (9)$$

Hence, by calculating the $F(R_\infty)$ magnitude by using the above equation and plotting $[F(R\infty)h\upsilon]^2$against hυ, it is possible to determine that the E_g. The required Eg is the optical band gap, and n is the constant corresponding to different types of electronic transitions.

Table 5. The lattice parameter, average force constant, porosity, poison ratio, stiffness constants, and elastic moduli.

Sample	a (exp) (A°)	K_{av} (nm^{-1})	Porosity (%)	σ	C11 (GPa)	C12 (GPa)	E (GPa)	G (GPa)	K (GPa)
NZ1	8.3376	172	15.8	0.27	205	104	117	46	137
NZ2	8.3455	171	15.3	0.272	204	107	111	43	139
NZ3	8.3349	170	19.1	0.259	203	107	106	42	139
NZ4	8.3429	169	17.5	0.265	201	105	109	43	137

Table 6. Density, wave accelerations, and Debye temperature.

Sample	ρ (exp) (Kg/m^3)	ρ (exp) (Kg/m^3)	V_l (m/sec)	V_s (m/sec)	V_m (m/sec)	θ_{DW} (K)
NZ1	5343	4497	6537	3718	4133	530
NZ2	5354	4536	6432	3543	3949	508
NZ3	5334	4316	6411	3692	4100	519
NZ4	5348	4412	6420	3661	4069	519

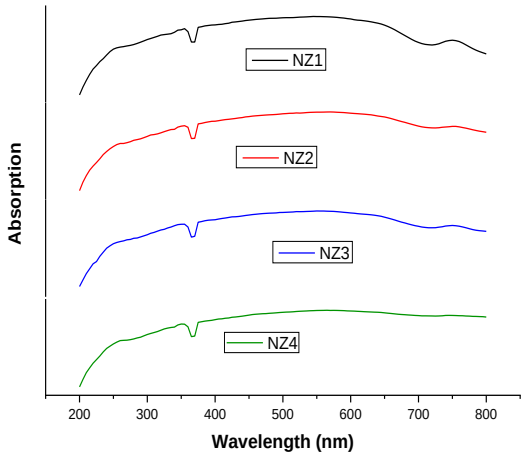

Fig. 8 UV-Vis-Absorption versus wavelength (nm)

Table 7. Bandgap variation with composition

Sample	Bandgap(eV)
NZ1	4.344
NZ2	4.124
NZ3	4.135
NZ4	4.273

Table 8. Magnetic behavior of NZF using VSM

Sample	Ms (emu/g)	Mr (emu/g)	Corecivity Hc (Oe)	Mr/Ms	Magnetic moment
NZ1	65.13	1.77	21.26	0.027	2.7568
NZ2	67.65	1.40	16.78	0.020	2.8634
NZ3	70.96	2.40	31.05	0.034	3.0035
NZ4	71.18	1.81	15.63	0.025	3.0128

The reduction in band gap due to copper doping and excess iron indicates an increase in sample conductivity due to the metallic properties of Cu^{2+} and Fe^{2+} ions due to the increased hopping mechanism.

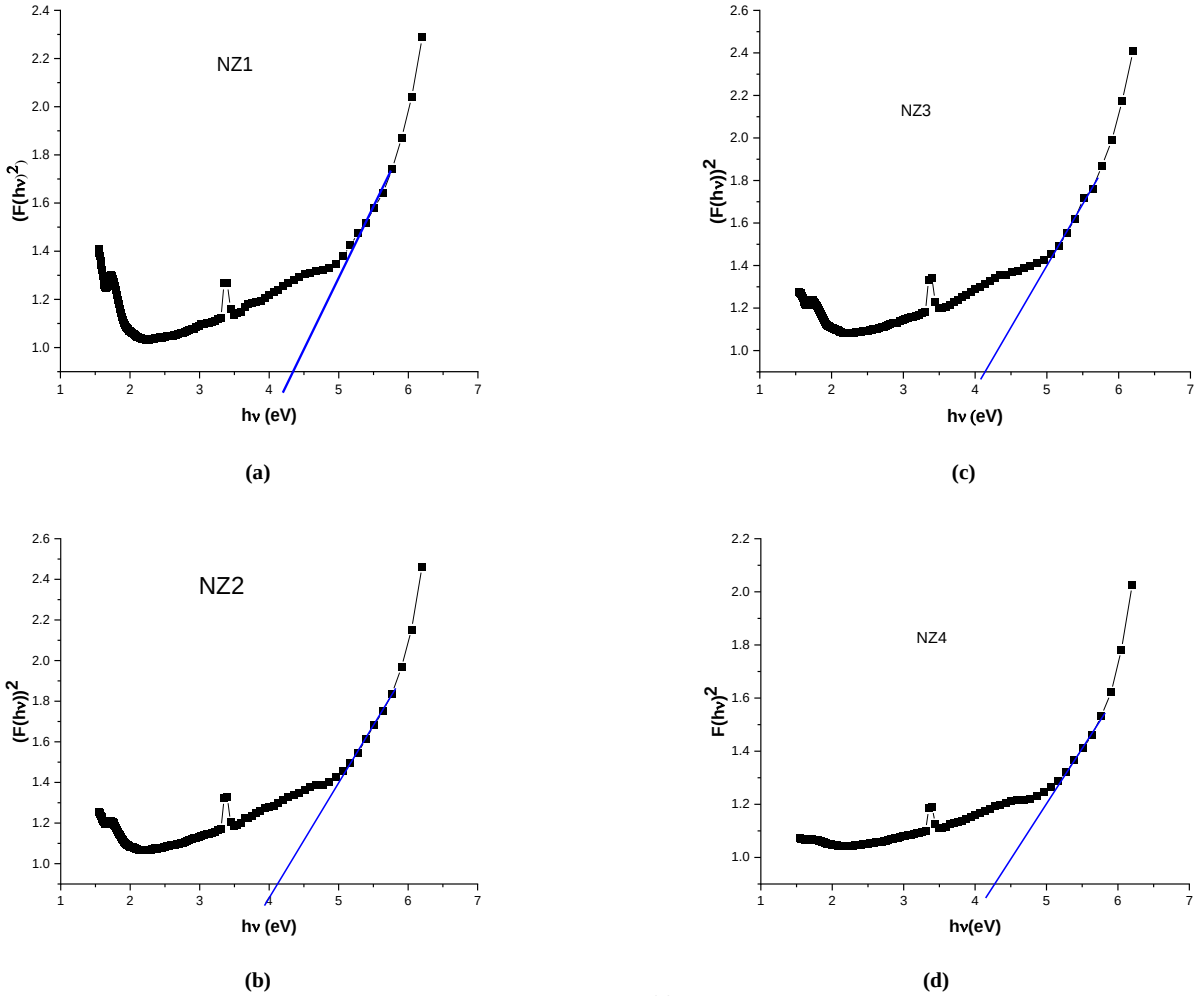

Fig. 9(a-d) Tauc's plots of ferrite samples

4.3. Magnetic Study

The magnetic behavior of NZF nanoparticles was investigated using VSM. Thin hysteresis loops reveal that the synthesized ferrites are soft and have low coercivity [34,35]. With copper doping, saturation magnetization has been observed to increase (figure 10).

The increase in saturation magnetization for copper doped and iron excess Ni-Zn ferrites compared to that of Ni-Zn ferrite shows that copper may be entering into A-sites and pushing Fe^{3+} ions to B-sites, thereby increasing the net magnetic moment. In the case of excess iron ferrite, since excess iron is doped in place of zinc ions, Fe^{2+} ions are formed at B-sites and transfer some of the nickel ions to A-sites leading to an increase in net magnetic moment. Although Ms is a bulk intrinsic material property[38], it was observed that M_r and M_r/M_s mirror tendency in H_c, despite the fact at a secondary scale. This is because Mr, although magnetization is also related to H_c, and affected by changes in microstructure, grain size and magnetic domain size, especially when near the single domain size. Mr follows a similar trend to that of Hc. These changes thus can be understood by estimating the dissemination of cations at A and B sites. For this purpose, Rietveld refinement has been done.

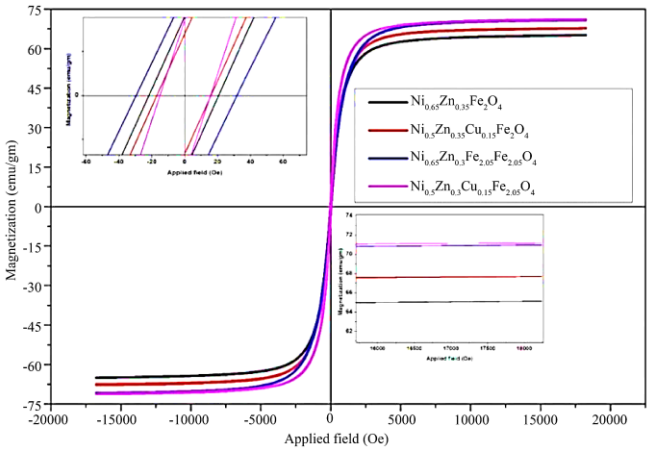

Fig. 10 Magnetic hysteresis of NZF nanoparticles

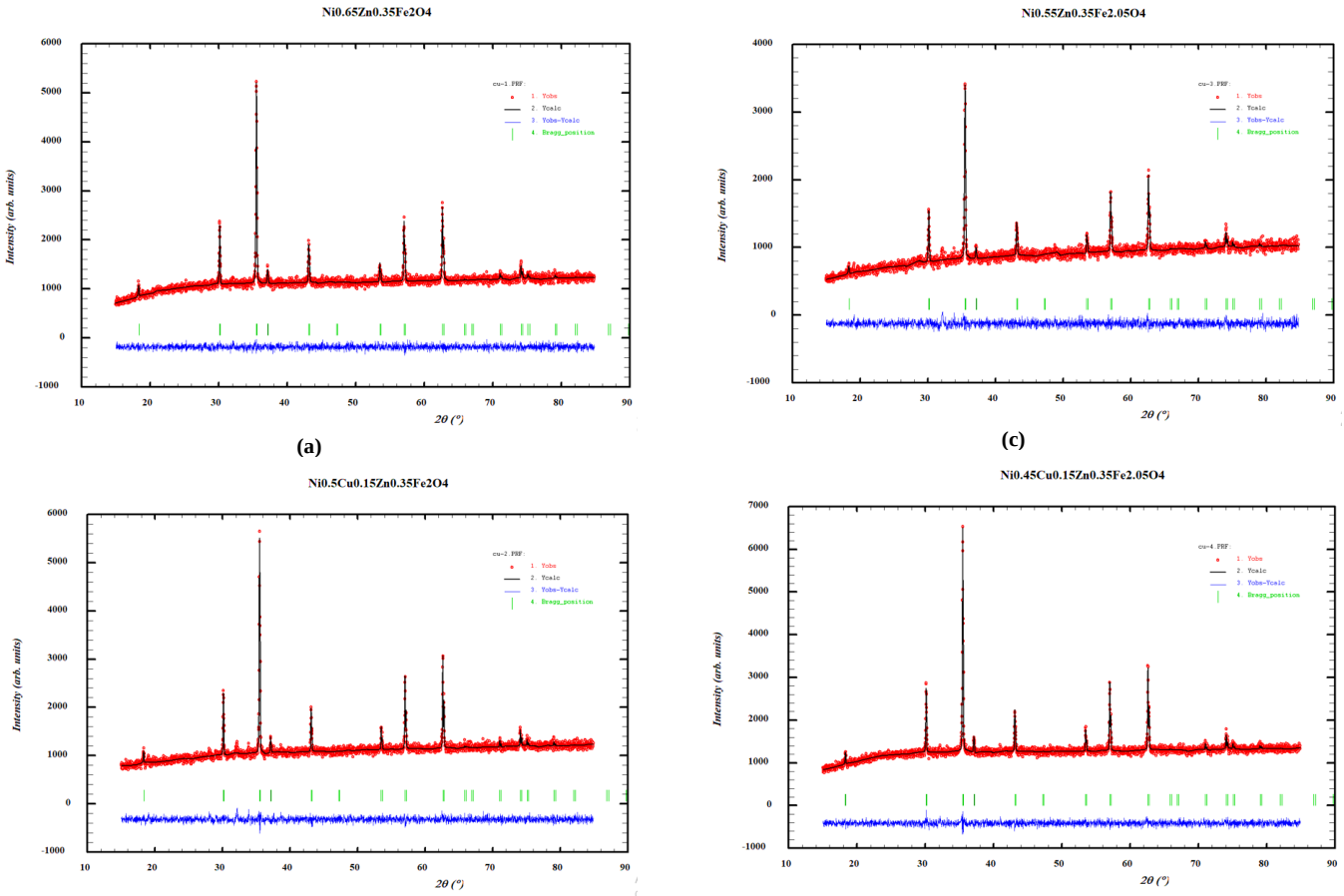

Fig. 11(a -d) Cation distribution (Rietveld Refinement) for the pellets i.e NZ1,NZ2,NZ3,NZ4

Table 9. Cation distribution of A-site & B-site for $NiZnCuFe_2O_4$

Sample	A-site			B-site				
	Zn	Fe	nA	Ni	Cu	Fe	nB	net moment
NZ1	0.35	0.65	3.25	0.65	0	1.35	8.05	4.8
NZ2	0.35	0.65	3.25	0.5	0.15	1.35	7.9	4.65
NZ3	0.3	0.7	3.5	0.65	0	1.4	8.3	4.8
NZ4	0.3	0.7	3.5	0.5	0.15	1.4	8.15	4.65

4.4. Cation Distribution (Rietveld Refinement)

The cation distribution in the FULLPROF suite is determined using the Rietveld refinement technique in this research [21]. The best information about the cation distribution is that the intensities are (i) largely self-sustained of oxygen parameter, (ii) change in the opposite direction of the cation distribution, and (iii)unchanged reflection experiments. It is very different. Table 9 shows the final cation distribution results of the Rietveld refinement analysis.

From fig-11(a-d), by employing the pretended cation dissemination, calculate the tetrahedral site boundary (r_A(cal)) and octahedral site boundary (r_B(cal)) using the relational expressions. The theoretical lattice constant (ath) is estimated by using the equation, calculated as:

$$a_{th} = \frac{8}{3\sqrt{3}}(r_A(cal) + r_o) + \sqrt{3}(r_{B(cal)} + r_o) \quad (9)$$

where r_0 is the radius of the oxygen ion and r_A and r_B are the ionic radii of the tetrahedral (A-site) and octahedral (B-site) sites. The lattice constant estimated from the above equations was close to the experimental value shown in Table 10.

Table 10. Average cations radius at tetrahedral (r_A) and octahedral (r_B) sites as a function of excess iron concentration(x) in $NiZnCuFe_2O_4$

Sample	R_A (A°)	R_B (A°)	a_{th}	$a_{Rietveld}$
NZ1	0.54653	0.66714	8.3661	8.3661
NZ2	0.54085	0.67115	8.3680	8.3680
NZ3	0.54863	0.66689	8.3687	8.3687
NZ4	0.53768	0.66645	8.3507	8.3507

Table 10 shows the values of the nickel-zinc ferrite samples observed, and we can see that the theoretical lattice constants are consistent with each other [7,8].As a result, the estimated distribution of cations shall be correct from Table 9; if iron ions occupy A and B positions, the magnetic strength is increased at A versus decreasing at B. As a result, the net magnetic field is reduced because of the difference in the magnetic field between B and A. Therefore, the use of copper instead of nickel ions increases the occupancy of iron ion occupancy at A-sites and reduces the magnetization.

Using XRD, FTIR, and Rietveld refinement analysis, it is observed that nearly about 10% of copper ions doped in Ni-Zn ferrites are migrated to A-sites which gives rise to instability in the occupancy of nickel and iron ions, predominantly in A-sites as well as B-sites.

5. Conclusion

Nickel zinc copper ferrite material has been developed and characterized. The pellets were prepared by using the co-precipitation process, which was sintered at 850°C for 4 hours. It was observed that the sensitivity levels are enhanced by 10% with reference to XRD, FTIR, UV-Vis, Raman, and VSM. From the XRD technique, diffraction peaks indicate a shift in sensitivity. Using Scherrer's formula, W-H charts, Size strain graphs, and Halder Wagner plots, the ferrite and spinel phase crystallite sizes were estimated. Due to their vibrational modes, the FTIR absorption spectra revealed the creation of a cubic spinel structure and revealed the locations of oxygen ions and their crystalline cations. The simultaneous redistribution of copper, nickel, and zinc ions at A and B sites was studied in the elasticity investigation. The predicted cation distribution was based on the projected copper distribution. These results show that at least 10% of copper ions are redirected to tetrahedral positions. As a result, nickel and zinc occupancies have distinct patterns. The fluctuation of nickel ions and 10% of the net doping concentration of copper at A sites is not a size-dependent phenomenon and may occur at greater particle sizes.

References

[1] Zeid A. ALOthman, "A Review: Fundamental Aspects of Silicate Mesoporous Materials," *Materials*, vol. 5, no. 12, pp. 2874-2902, 2012. [CrossRef] [Google Scholar] [Publisher Link]

[2] Mritunjoy Prasad Ghosh et al., "Tuning the Microstructural, Optical and Superexchange Interactions with Rare Earth Eu Doping in Nickel Ferrite Nanoparticles," *Materials Chemistry and Physics*, vol. 241, 2020. [CrossRef] [Google Scholar] [Publisher Link]

[3] Mohammad Abu Haija et al., "Adsorption and Gas Sensing Properties of CuFe2O4 Nanoparticles," *Materials Science-Poland*, vol. 37, no. 2, pp. 289-295, 2019. [CrossRef] [Google Scholar] [Publisher Link]

[4] Ritu Malik et al., "Functional Gas Sensing Nanomaterials: A Panoramic View," *Applied Physics Reviews*, vol. 7, p. 021301, 2020. [CrossRef] [Google Scholar] [Publisher Link]

[5] Rohit R. Powar et al., "Effect of Zinc Substitution on Magnesium Ferrite Nanoparticles: Structural, Electrical, Magnetic, and Gas-Sensing Properties," *Materials Science & Engineering B*, vol. 262, p. 114776, 2020. [CrossRef] [Google Scholar] [Publisher Link]

[6] M.K. Anupama, B. Rudraswamy, and N. Dhananjaya, "Investigation on Impedance Response and Dielectric Relaxation of Ni– Zn Ferrites Prepared by Self-Combustion Technique," *Journal of Alloys and Compounds*, vol. 706, pp. 554-561, 2017. [CrossRef] [Google Scholar] [Publisher Link]

[7] Yuandong Peng et al., "Fe-Based Soft Magnetic Composites Coated with Nizn Ferrite Prepared by a Coprecipitation Method," *Journal of Magnetism and Magnetic Materials*, vol. 428, pp. 148-153, 2016. [CrossRef] [Google Scholar] [Publisher Link]

[8] Defi Yuliantika et al., "Exploring Structural Properties of Cobalt Ferrite Nanoparticles from Natural Sand," *IOP Conference Series: Materials Science and Engineering*, vol. 515, p. 012047, 2019. [CrossRef] [Google Scholar] [Publisher Link]

[9] Pradeep Chavan, "Facile Synthesis, Diffused Reflectance Spectroscopy & Fluorescence Studies of $Ni_{0.5-x}Mg_{0.5}Cu_xFe_2O_4$ Nanoparticles," *Journal of Fluorescence*, vol. 31, pp. 1023–1028, 2021. [CrossRef] [Google Scholar] [Publisher Link]

[10] U. Naresh, R. Jeevan Kumar, and T. Ram Parasad, "Optical Properties of Copper Ferrite Nano-Particle Synthesized via Hydrothermal Technique," *Bulletin of Pure and Applied Sciences*, vol. 37-D, no. 2, 2018. [CrossRef] [Google Scholar] [Publisher Link]

[11] S. K. Joshi et al., "Optical Spectra and Energy Band Gap of Ni–Zn Ferrite," *IEEE Transactions on Magnetics*, vol. 37, no. 4, 2001. [CrossRef] [Google Scholar] [Publisher Link]

[12] S. A. Mazen, and T. A. Elmosalami, "Structural and Elastic Properties of Li-Ni Ferrite," *International Scholarly Research Network ISRN Condensed Matter Physics*, vol. 2011, 2011. [CrossRef] [Google Scholar] [Publisher Link]

[13] T. Yu et al., "Cation Migration and Magnetic Ordering in Spinel Cofe2o4 Powder: Micro-Raman Scattering Study," *Journal of Physics Condensed Matter*, vol. 14, no. 37, p. L613, 2002. [CrossRef] [Google Scholar] [Publisher Link]

[14] Noppakun Sanpo, Christopher C. Berndt, and James Wang, "Microstructural and Antibacterial Properties of Zinc-Substituted Cobalt Ferrite Nanopowders Synthesized by Sol-Gel Methods," *Journal of Applied Physics*, vol. 112, p. 084333, 2012. [CrossRef] [Google Scholar] [Publisher Link]

[15] J. N. Pavan Kumar Chintala et al., "Impact of Cobalt Substitution on Cation Distribution and Elastic Properties of Ni-Zn Ferrite Using X-Ray Diffraction, Infrared and Mössbauer Spectral Analysis," *Journal of Physics and Chemistry of Solids*, 2021. [CrossRef] [Google Scholar] [Publisher Link]

[16] Brajesh Nandan, M.C. Bhatnagar, and Subhash C. Kashyap, "Cation Distribution in Nanocrystalline Cobalt Substituted Nickel Ferrites: X-Ray Diffraction and Raman Spectroscopic Investigations," *Journal of Physics and Chemistry of Solids*, vol. 129, pp. 298-306, 2019. [CrossRef] [Google Scholar] [Publisher Link]

[17] S.Ashmitha Sailish et al., "SbO2 Nanoparticles: Structural, Morphological and Optical analysis for Photocatalytic Applications," *SSRG International Journal of Applied Physics*, vol. 6, no. 2, pp. 28-30, 2019. [CrossRef] [Publisher Link]

[18] A.B. Murphy, "Band-gap Determination from Diffuse Reflectance Measurements of Semiconductor Films, and Application to Photoelectrochemical Water-Splitting," *Solar Energy Materials and Solar Cells*, vol. 91, pp. 1326-1337, 2007. [CrossRef] [Google Scholar] [Publisher Link]

[19] Alfred A. Christy, Olav M. Kvalheim, and Rance A. Velapoldi, "Quantitative Analysis in Diffuse Reflectance Spectrometry: A Modified Kubelka-Munk Equation," *Vibrational Spectroscopy*, vol. 9, pp. 19-27, 1995. [CrossRef] [Google Scholar] [Publisher Link]

[20] Debojyoti Nath, Fouran Singh, and Ratan Das, "X-ray Diffraction Analysis by Williamson-Hall, Halder-Wagner and Size-Strain Plot Methods of Cdse Nanoparticles - A Comparative Study," *Materials Chemistry and Physics*, vol. 239, p. 122021, 2020. [CrossRef] [Google Scholar] [Publisher Link]

[21] H. Mkaddem et al., "Anti-Inflammatory Drug Diclofenac Removal by a Synthesized Mgal Layered Doublehydroxide," *Journal of Molecular Liquids*, vol. 359, p. 119207, 2022. [CrossRef] [Google Scholar] [Publisher Link]

[22] J.N. Pavan Kumar Chintala et al., "Impact of Cobalt Substitution on Cation Distribution and Elastic Properties of Ni–Zn Ferrite Investigated by X- Ray Diffraction, Infrared Spectroscopy, and Mössbauer Spectral Analysis," *Journal of Physics and Chemistry of Solids*, vol. 160, 2021. [CrossRef] [Google Scholar] [Publisher Link]

[23] J. N. Pavan Kumar Chintala et al., "An Accurate Low-Temperature Cation Distribution of Nano Ni-Zn Ferrite Having a Very High Saturation Magnetization," *Journal of Superconductivity and Novel Magnetism*, vol. 34, pp. 149–156, 2021. [CrossRef] [Google Scholar] [Publisher Link]

[24] D. R. S. Gangaswamy et al., "Enhanced Magnetic Permeability in $Ni_{0.55-y}Co_yZn_{0.35}Mg_{0.10}Fe_2O_4$ Synthesized by Sol-Gel Method," *Journal of Superconductivity and Novel Magnetism*, vol. 31, pp. 3753–3760, 2018. [CrossRef] [Google Scholar] [Publisher Link]

[25] S.F. Mansour, M.A. Abdo, and F.L. Kzar, "Effect of Cr Dopant on the Structural, Magnetic and Dielectric Properties of Cu-Zn Nanoferrites," *Journal of Magnetism and Magnetic Materials*, vol. 465, pp. 176-185, 2018. [CrossRef] [Google Scholar] [Publisher Link]

[26] M.A. Ahmed et al., "Structural and Electrical Studies on La^3^+ Substituted Ni-Zn Ferrites," *Materials Chemistry & Physics*, vol. 92, no. 2-3, pp. 310-321, 2005. [CrossRef] [Google Scholar] [Publisher Link]

[27] Arvind Varma et al., "Solution Combustion Synthesis of Nanoscale Materials," *Chemical Reviews*, vol. 116, no. 23, pp. 14493-14586, 2016. [CrossRef] [Google Scholar] [Publisher Link]

[28] S.L.Meena, "Spectral and Thermal Properties of Ho3+ Doped Aluminum- Barium- Calcium-Magnesium Fluoride Glasses," *SSRG International Journal of Applied Physics*, vol. 7, no. 1, pp. 14-20, 2020. [CrossRef] [Publisher Link]

[29] A. D. Patil et al., "Elastic, Impedance Spectroscopic and Dielectric Properties of Tio Doped Nanocrystalline Nicuzn Spinel Ferrites," *Phase Transitions*, vol. 92, no. 9, pp. 790-797, 2019. [CrossRef] [Google Scholar] [Publisher Link]

[30] B. Rajesh Babu et al., "Structural and Magnetic Properties of Ni0.5Zn0.5alxfe2−X O4 Nano Ferrite System," *Materials Chemistry and Physics*, vol. 148, no. 3, pp. 585-591, 2014. [CrossRef] [Google Scholar] [Publisher Link]

[31] T.R. Tatarchuk et al., "Effect of Cobalt Substitution on Structural, Elastic, Magnetic and Optical Properties of Zinc Ferrite Nanoparticles," *Journal of Alloys and Compounds*, vol. 731, pp. 1256-1266, 2018. [CrossRef] [Google Scholar] [Publisher Link]

[32] Juhang Yin et al., "Power Controlled Microstructure and Infrared Properties of Air Plasma Spraying Based on YSZ Coatings," *Surface and Coatings Technology*, 2021. [CrossRef] [Google Scholar] [Publisher Link]

[33] Marc A. Meyers et al., "Shear Localization in Dynamic Deformation of Materials: Microstructural Evolution and Self-Organization," *Materials Science & Engineering A*, vol. 317, no. 1-2, pp. 204-225, 2001. [CrossRef] [Google Scholar] [Publisher Link]

[34] P. Priyadharshini, and K. Pushpanathan, "Tuning of Crystallite Size, Energy gap and Magnetic Property of Mn doped CoFe O Nanoparticles," *Surface Review and Letters*, vol. 28, no. 6, 2021. [CrossRef] [Google Scholar] [Publisher Link]

[35] Sagar M. Mane et al., "Correlative Structural Refinement-Magnetic Tunability, and Enhanced Magnetostriction in Lowtemperature, Microwave- Annealed, Nisubstituted Cofe2o4 Nanoparticles," *Journal of Alloys and Compounds*, vol. 895, p. 162627, 2021. [CrossRef] [Google Scholar] [Publisher Link]

[36] A.A. Sattar et al., "Improvement of the Magnetic Properties of Mn-Ni-Zn Ferrite by the Non-magnetic Al3+-Ion Substitution," *Journal of Applied Sciences*, vol. 5, no. 1, pp. 162-168, 2005. [Google Scholar] [Publisher Link]

[37] M. Chaitanya Varma, S. Bharadwaj, and K. Vijaya Babu, "Observation of Anomalous Site Occupancy in Ni-Co-Cu-Cr Ferrite System Synthesized by Sol-Gel Method," *Physica B: Condensed Matter*, 2019. [CrossRef] [Google Scholar] [Publisher Link]

[38] V. Lakshmi Savithri Vatsalya et al., "Evidence of Superparamagnetism in Nano Phased Copper Doped Nickel Zinc Ferrites Synthesized by Hydrothermal Method," *Optik*, vol. 247, p. 167874, 2021. [CrossRef] [Google Scholar] [Publisher Link]

[39] V.K. Lakhani et al., "Structural Parameters and X-Ray Debye Temperature Determination Study on Copperferrite-Aluminates," *Solid State Sciences*, vol. 13, no. 3, pp. 539-547, 2011. [CrossRef] [Google Scholar] [Publisher Link]

[40] Amrin R.Kagdia et al., "Influence of Mg Substitution on Structural, Magnetic and Dielectric Properties of X-Type Bariumsingle Bondzinc Hexaferrites $Ba_2Zn_{2-x}Mg_xFe_{28}O_{46}$," *Journal of Alloys and Compounds*, vol. 741, pp. 377-391, 2018. [CrossRef] [Google Scholar] [Publisher Link]

[41] [Online]. Available: https://www.ill.eu/sites/fullprof/

[42] R. Tauc, Grigorovici, and A. Vancu, "Optical Properties and Electronic Structure of Amorphous Germanium," *Physica Status Solidi*, vol. 15, pp. 627-637, 1966. [CrossRef] [Google Scholar] [Publisher Link]

[43] Mehjabeen Khan et al., "X-Ray Analysis of $BaTiO_3$ Ceramics by Williamson-Hall and Size Strain Plot Methods," *AIP Publishing*, 2019. [CrossRef] [Google Scholar] [Publisher Link]